Chapter 3

Background radiation and shielding

3.1 Introduction

In contrast to previous and existing colliders, the dominant primary source of background radiation at the LHC, when operating at design luminosity, arises from collisions at the interaction point. The rates expected from beam-halo particles and beam-gas interactions are negligible in comparison. In the inner detector, charged hadrons from inelastic proton-proton interactions dominate the radiation backgrounds at small radii, while the effects of other backgrounds, such as neutrons, become more important further out (see [34] for detailed studies of the various radiation sources, radiation levels, neutron fluences and activation levels expected in ATLAS throughout the lifetime of the experiment).

In ATLAS, most of the energy from the primary particles is dumped into two regions: the Target Absorber Secondaries (TAS) collimators, and the Forward Calorimeters (FCal) depicted in figure 3.1, which are therefore among the strongest sources of secondary radiation. These two sources are somewhat self-shielding, and since they are compact, they have been further shielded with layers of dense material and cladding. The beam-vacuum system, on the other hand, spans the whole length of the detector. In the forward regions, it is another major source of radiation background due to interactions of primary particles which strike the beam-pipe at very shallow angles. Through this mechanism, the beam-pipe becomes an extended line source illuminating the interior of the forward cavity. Detailed studies have shown that the beam-line material is responsible for more than half of the fluences expected in the muon system [34].

A thorough understanding of the impact of background radiation has been a critical element in the design phase of most of the components of the detector and a number of deleterious effects have been considered:

1. Increased detector occupancy may be an issue. In tracking detectors, this can lead to inefficiencies, degraded resolutions, and increased rates of fake tracks. In calorimeters, the pile-up fluctuations at high luminosity degrade the energy resolution.

2. Hits generated by slow neutrons dominate the occupancy of the muon spectrometer system. This effect has not been of any concern at previous colliders.

2008 JINST 3 S08003

3. Spurious trigger rates will increase if the background radiation consists of penetrating tracks. Also, increased occupancies can increase the rates of random triggers.

4. Radiation may damage silicon detectors and readout electronics.

5. Interactions leading to anomalous deposits of local radiation can change the logical status of electronic signals (single-event upset) or permanently destroy components (single-event damage).

6. Wire detectors can experience “ageing” (reduced gain and therefore efficiency) due to polymerised deposits on the wires caused by radiation interacting with certain components of the detector gas.

7. The large fluences expected at the LHC design luminosity may lead to a significant radiation hazard from the prompt component of the radiation, when the accelerator is operating.

8. Nuclear interactions in dense materials will lead to the creation of residual radio-nuclides. The resulting dose rates from radio-activation of certain materials will lead to radiological hazards, which impact access and maintenance scenarios.

The largest impact from background radiation is of course to be expected close to the beam-pipe, in particular in the region of the inner detector and the forward calorimeters. Given the lack of available space and the large contribution from primaries, only a limited amount of moderator shielding could be installed to minimise the impact of background radiation, as described in section 3.2.

Very large reductions in the expected background rates in the muon spectrometer have been achieved by designing a large amount of shielding around the TAS. A total shielding weight of 2825 tonnes (1887 tonnes of metal, 920 tonnes of concrete, and 18 tonnes of plastic) has thus been added to the detector. Since different types of radiation are best stopped with different types of shielding materials, a multi-layered shielding approach has been used. The inner layer's purpose is to stop high-energy hadrons and their secondaries. This layer is made of materials such as iron or copper, which provide a large number of interaction lengths. In the case of iron, studies have shown that a minimum carbon content of a few percent is advantageous since it efficiently moderates the neutron energies down to lower values. A second layer, consisting of boron-doped polyethylene, is used to moderate the neutron radiation escaping from the first layer and the low-energy neutrons are then captured by the dopant. Photon radiation is created in the neutron-capture process and these photons are stopped in the third shielding layer which consists of steel or lead. Lead is more effective in stopping photons, but induces more neutron radiation than steel. Figure 3.1 shows the locations of the different shielding components in ATLAS.

3.2 Description of the shielding

The moderator shielding (figure 3.2a) on the front face of each of the end-cap and forward LAr calorimeters reduces the neutron fluences in the volume of the inner detector by protecting the inner detector from back-splash of neutrons from the calorimeter. It is made of polyethylene,

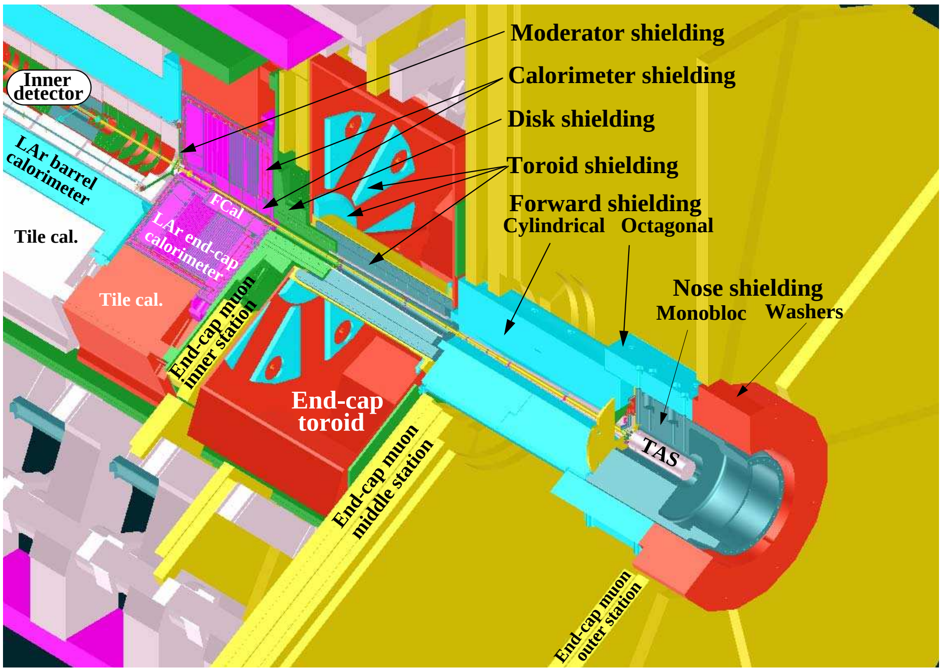

Figure 3.1: Schematic view of major ATLAS detector systems and of the main shielding components (see text).

doped with 5% boron in the form of B_4C. Reactor tests have demonstrated that this choice for the dopant results in a plastic which is more radiation-hard than if other boron dopants had been used. This is important since the shielding in front of the forward calorimeters is exposed to a very large ionising dose over the lifetime of the ATLAS experiment.

There are three brass shielding elements inside each of the end-cap calorimeter cryostats, located directly behind the calorimeters (figure 3.2b). The largest one is attached to the rear end-plate of the cryostats and has a diameter of 387 cm. Closer to the beam-line are two other shielding plugs. One of these is a cylindrically-shaped extension of the forward calorimeters. The main purpose of these shielding elements is to protect the end-cap inner muon stations from the background radiation.

The next protection element is the shielding disk (figure 3.2c), which serves in fact a threefold purpose: it supports the muon chambers in the first end-cap muon station, it shields these chambers from background radiation emerging from the calorimeters, and it provides a well-defined path for the magnetic field flux return from the solenoid magnet. The bulk of this shielding disk consists of a vertical steel disk with a diameter of 872 cm. This disk supports end-cap muon trigger chambers (see section 6.8). At the centre of the disk and surrounding the beam-pipe is a stainless steel tube containing a set of cylindrical shielding pieces made of leaded red brass (85% Cu, 5% Pb, 5% Sn, 5% Zn). This tube also supports Cathode Strip Chambers (CSC) and Monitored Drift Tubes (MDT). Brass shielding has been added to the disk in order to protect the CSC chambers. There is a polyethylene layer on the outside of this brass shielding, which is doped with B_2O_3, to moderate the neutrons, while photons created in the neutron absorption process are stopped in a third layer made of lead.

2008 JINST 3 S08003

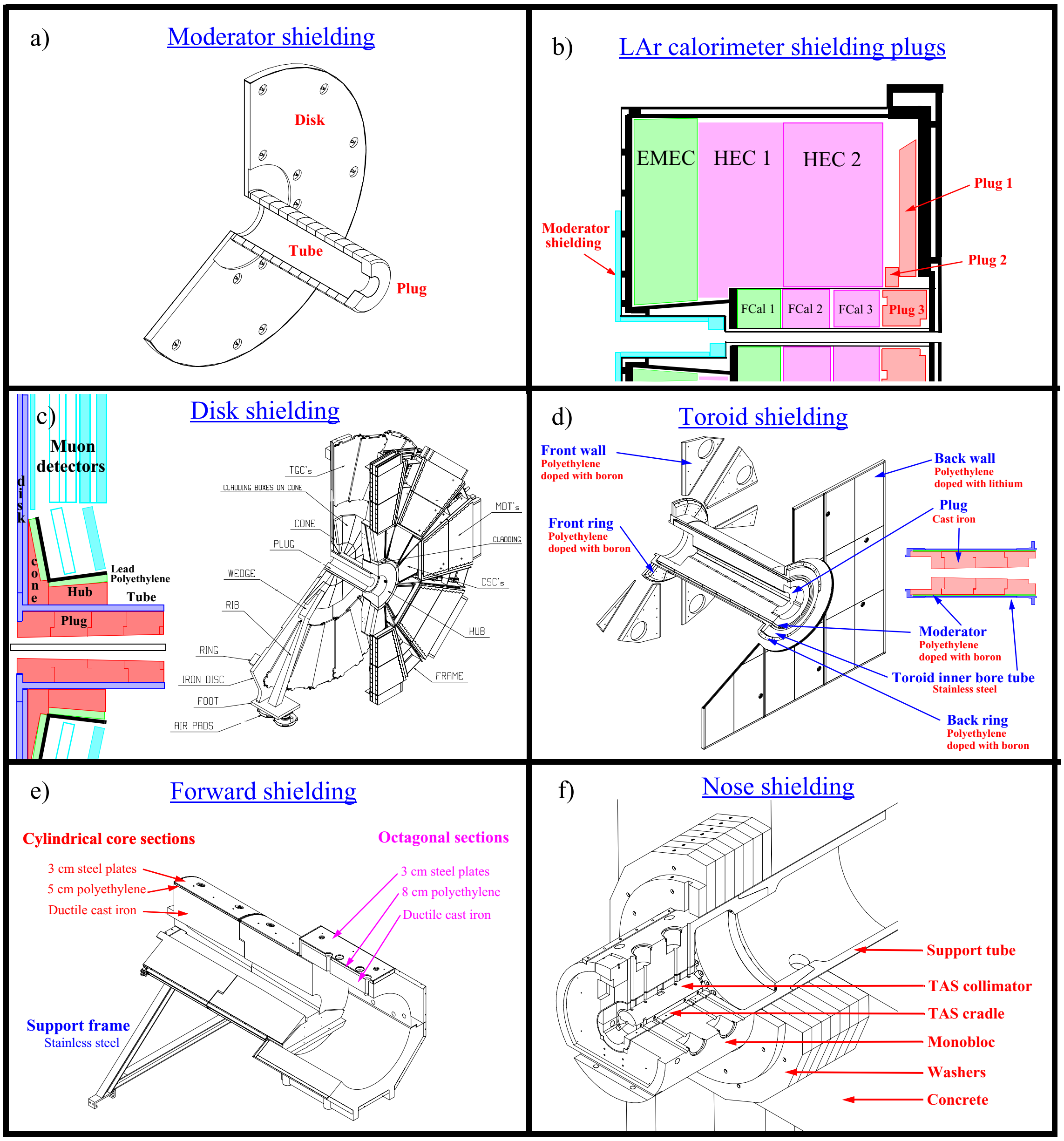

Figure 3.2: Details of the shielding components as described in the text: a) moderator, b) LAr calorimeter plugs, c) disk, d) toroid, e) forward, and f) nose shielding.

The next protection element is the end-cap toroid shielding (figure 3.2d), which consists of two parts, one located outside the toroid and enclosing the beam-pipe and one inside the cryostat:

- the first one is a cylindrical structure made of ductile cast iron, which surrounds the beam-pipe on the inside of the two end-cap toroid cryostats. The front piece has a large hole in the centre, into which the stainless steel tube of the shielding disk fits. On the outside of the cast iron is a polyethylene layer doped with B_2O_3 (5%). The photons created in the polyethylene layer are stopped by the stainless-steel bore tube, which supports the shielding in the end-cap toroid;

- the second part of the toroid shielding consists of various polyethylene structures, which are located in the vacuum of the end-cap toroid cryostats. The polyethylene is doped with B_4C, which causes fewer out-gassing problems than other dopants. Photons created when the neutrons are absorbed by the boron are stopped by the aluminium of the cryostat itself.

The purpose of the two forward shielding assemblies (figure 3.2e) is to protect the middle and outer end-cap muon stations from background particles created in secondary interactions in the beam-pipe, the calorimeters and the TAS collimators. These shielding elements, which are removable and will be stored in the surface building during maintenance of ATLAS, consist of two parts: a cylindrical core and a set of octagonal pieces in the rear. All pieces are made of cast ductile iron, surrounded by a layer of polyethylene doped with boron in the form of H_3BO_3 and followed by a 3 cm thick steel layer. The core pieces are enclosed in a 5 cm thick polyethylene layer, while an 8 cm thick layer surrounds the octagonal pieces. These polyethylene layers are made of 10,000 bricks of three different shapes.

The final shielding element, or nose shielding as depicted in figure 3.2f, supports the TAS collimator and protects ATLAS from the radiation created in this collimator, which is designed to prevent the first LHC quadrupole from quenching due to the energy deposited by the particles emerging from the interactions in ATLAS. The nose shielding is permanently installed in ATLAS and, unlike the forward shielding assemblies, cannot be removed during shutdowns. The main component of this shielding is the cylindrical 117 tonne heavy "monobloc", which has an outer diameter of 295 cm. It is made of cast iron and supported by a tube, which is anchored in a 460 tonne concrete structure. The 200 tonne heavy "washers", which are located around the support tube, increase the radial thickness of the iron shielding by 112 cm in a region where the monobloc is thin.

3.3 Calculation of particle fluences and absorbed doses

A vast and systematic effort has been made in the design phase to optimise the shielding in ATLAS by using different simulation programs [34] for simulating hundreds of different geometrical options. These studies have required significant computing resources, since the secondary particles in the hadronic showers had to be followed down to very low energies. Different event generators and transport codes have been used in an attempt to assess the systematic uncertainties in the calculations. When optimising the shielding configuration and materials in the limited space available in ATLAS, it was very often necessary to make trade-offs between different background types, e.g. neutrons versus photons. It has therefore been quite important to also understand the detector response to different types of background radiation, typically particles in the MeV range, in order to converge to the optimal solution [35, 36].

The expected particle fluences (integrated over energy) agree to typically better than 20%, as was shown by comparing two of the most commonly used minimum-bias event generators, PHOJET1.12 [37–39] and PYTHIA6.2 [40]. Larger differences of up to 50% were observed for pions, kaons, and muons with energies above several GeV. However, these particles provide only a small contribution to the total fluence. The program most used for the shielding optimisation in ATLAS has been the GCALOR package [41], which contains the CALOR code [42] with an interface to

2008 JINST 3 S08003

GEANT3 [43]. FLUKA2001 [44] is another transport code, which is widely used for studies of hadronic and electromagnetic cascades induced by high-energy particles, and which has been extensively used in simulations of background radiation in ATLAS. In order to investigate transport-code differences, GCALOR was compared not only to FLUKA but also to MARS14(2002) [45]. Comparisons for simplified geometries as well as for the most detailed descriptions of the detector have been carried out.

The results of these studies are extensively reported in [34]: the overall conclusion is that the predictions of FLUKA, MARS and GCALOR are in good agreement for energy-integrated neutron, charged hadron, photon and e^+e^- fluences. For most regions in the inner detector, the difference between the FLUKA and GCALOR values is below 40%. In the pixel vertexing layer differences as large as 80% are however observed for charged hadrons. An excellent agreement, typically to within 20%, between the respective photon and neutron fluences in the muon spectrometer is observed when comparing the FLUKA and the GCALOR results. The charged hadron and lepton fluences in the muon spectrometer show much larger discrepancies, but the differences are always within a factor of 2.5. An overall safety factor of five has been used in the design of the ATLAS muon spectrometer.

The absorbed dose is the mean energy deposited per unit mass, taking into account all energy-loss mechanisms (but corrected for rest-mass effects). The dominant energy-loss mechanism is usually ionisation, but non-ionising energy loss is also important for understanding detector and electronic damage effects. The ionising dose is defined in the following as the integrated dE/dx energy loss in the detector material from charged particles, excluding ionisation energy loss from nuclear recoils. It is given in units of Gy/y, where one year corresponds to 8×10^{15} inelastic proton-proton collisions (assuming an inelastic cross-section of 80 mb, a luminosity of 10^{34} cm^{-2} s^{-1} and a data-taking period of 10^7 s). Comparisons of the calculated ionising dose in the inner detector between FLUKA and GCALOR show differences of up to a factor of two.

3.3.1 The inner-detector and calorimeter regions

Figure 3.3 shows a GCALOR calculation of the ionising dose in the region closest to the interaction point. The forward calorimeters will be exposed to up to 160 kGy/y, whereas the corresponding number for the end-cap electromagnetic calorimeters is 30 kGy/y. This will lead to very large integrated doses over the full lifetime of the experiment and is one of the main reasons why only the LAr technology with its intrinsically high resistance to radiation is used in the end-cap and forward regions. The main concern in the design phase has been for the electrode materials, primarily polymers such as polyimide, which had to be chosen with care and thoroughly tested for radiation hardness [46, 47].

The tile calorimeter, with its scintillator samplings read out by wavelength-shifting fibres, is protected by the LAr electromagnetic calorimeter and is exposed to less than 30 Gy/y, i.e. 5,000 times less than the forward calorimeters. The scintillators and fibres were nevertheless also thoroughly studied under irradiation [48–51] in order to determine their degradation during the lifetime of ATLAS.

In the inner detector, a very large effort had to be devoted over many years to the understanding of the impact of irradiation on silicon sensors, on front-end electronics circuits and on ageing phenomena in the ionising gas used for the straw tubes.

2008 JINST 3 S08003

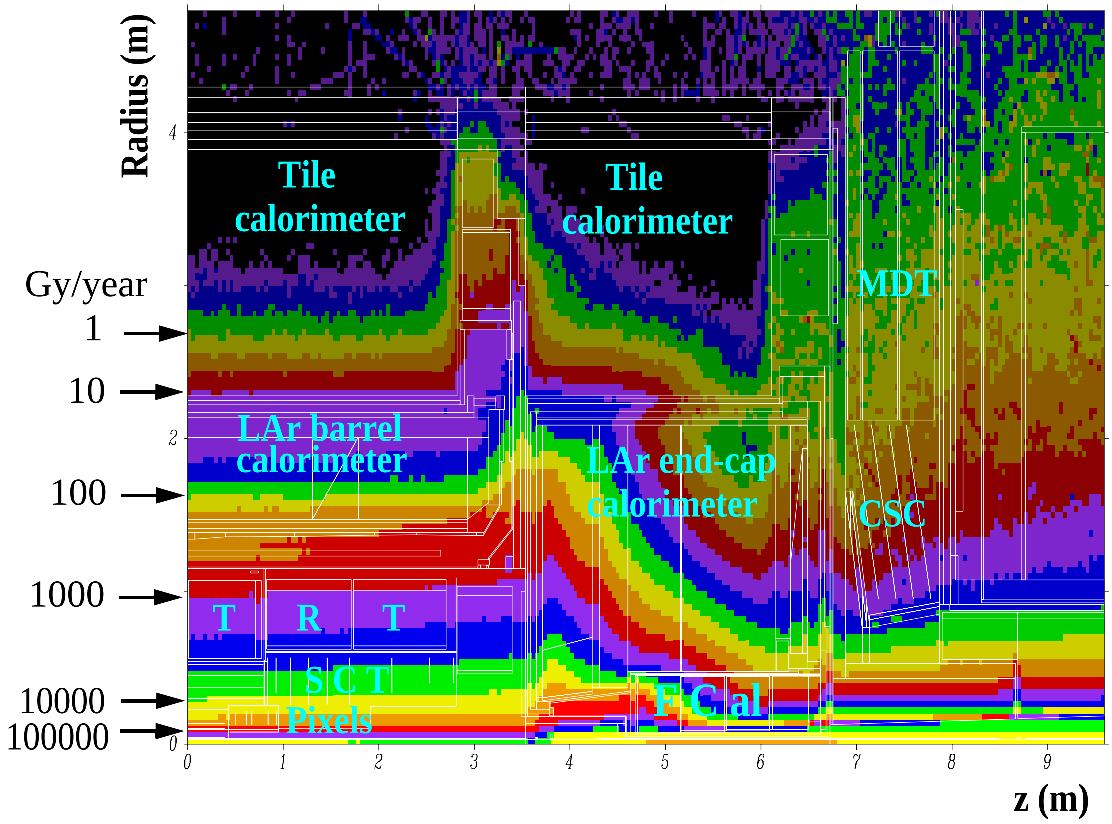

Figure 3.3: The total ionising dose per year calculated by GCALOR (see text) in one quarter of the central part of the detector. The locations of the inner detector sub-systems, of the different calorimeters and of the inner end-cap muon stations are indicated. The scale on the left gives the integrated dose per year corresponding to the various iso-lines.

Two main mechanisms lead to the degradation of the performance of silicon devices under irradiation. First, there is the effect of damage to the devices due to ionising energy loss. This can lead to the creation of trapped charges, in particular in the oxide layer of the sensor, which alters its electric properties. The second effect is bulk damage, or displacement damage, which is caused by the displacement of silicon atoms in the lattice. In the study of bulk damage to silicon devices, it is useful to introduce a quantity called the 1 MeV neutron equivalent fluence (F_{neq}). This fluence is obtained by convoluting the various particle energy spectra and fluences with silicon displacement-damage functions, normalised using the non-ionising energy loss (NIEL) cross-sections to the expected damage of 1 MeV neutrons [52].

Table 3.1 lists the particle rates, F_{neq} values and ionising doses predicted by FLUKA in the inner detector regions shown in figure 3.3. In the pixel detector, the particle rates are dominated by charged pions and photons. The latter are produced mostly in neutron capture processes but also directly from the primary collisions and from interactions in the beam-pipe and its related equipment. The predicted ionising dose in the innermost layer of the barrel pixel detector is 160 kGy/y,

Table 3.1: Particle rates, fluences and doses in key locations of the inner detector sub-systems (see figure 4.2 for the definitions and positions of the inner detector layers). Here, F_{neq} is the 1 MeV neutron equivalent fluence (see text). The FLUKA program has been used for this calculation and the statistical uncertainties are typically less than 10%. One year corresponds to 8×10^{15} inelastic proton-proton collisions (assuming an inelastic cross-section of 80 mb, a luminosity of 10^{34} cm^{-2} s^{-1} and a data-taking period of 10^7 s).

Region	R (cm)	Particle rates (kHz/cm^2)						F_{neq} ($\times 10^{+12}$ cm^{-2})	Ionisation dose (Gy/y)
		γ	Protons	Neutrons	$\pi^{\pm}$	$\mu^{\pm}$	e^{-}		
		> 30 keV	> 10 MeV	> 100 keV	> 10 MeV	> 10 MeV	> 0.5 MeV		
Pixel layer 0	5.05	45800	2030	4140	34100	300	8140	270	158000
Pixel layer 2	12.25	9150	280	1240	4120	190	1730	46	25400
SCT barrel layer 1	29.9	4400	80	690	990	130	690	16	7590
SCT barrel layer 4	51.4	3910	36	490	370	67	320	9	2960
SCT end-cap disk 9	43.9	7580	73	840	550	110	470	14	4510
TRT outer radius	108.0	2430	10	380	61	7	53	5	680

which is the same as for the forward calorimeter, while the F_{neq} is expected to be 3×10^{14} cm^{-2}/y. In the SCT detector, the charged hadron and neutron rates are comparable and the F_{neq} and the ionising dose are reduced by about a factor of 20 with respect to the first pixel layer.

While most of the charged hadrons originate from the interaction point, most of the neutrons in the inner detector are the result of albedo (back-splash from the calorimeters). The purpose of the moderator shielding described in section 3.2 is to moderate the neutrons from the end-cap and forward calorimeters to lower their energies to values for which their contribution to the total F_{neq} is minimised. The polyethylene in the moderator shielding is doped with boron, which has a large cross-section for the capture of thermal neutrons. Nevertheless, the inner detector cavity will be filled during LHC operation by an almost uniform "gas" of thermal neutrons with a flux of 1–2 MHz/cm^2 and the sensitive detectors will be exposed to fluxes of 2–10 MHz/cm^2 of low-energy photons originating from the interactions themselves and from neutron capture. The dominant long-term impact of these particle fluences is not only radiation damage but also activation of the detector components (see section 3.5).

3.3.2 The muon spectrometer region

The effects of the absorbed ionising dose in the most critical muon spectrometer regions have been studied [53]. The CSC's in the inner end-cap stations will be exposed to the highest dose. Figure 3.3 shows that in this region the ionising dose will vary between 3 and 20 Gy/y. The chambers closest to the beam-line in the middle end-cap stations are expected to see at most 10 Gy/y. Most of the muon spectrometer will, however, be exposed to less than 1 Gy/y.

Although care had also to be applied to the choices of materials, to the design of the front-end electronics circuits and to the choice of the ionising gases for all the muon chamber technologies, radiation damage due to the ionising dose is not the only concern in the muon spectrometer region.

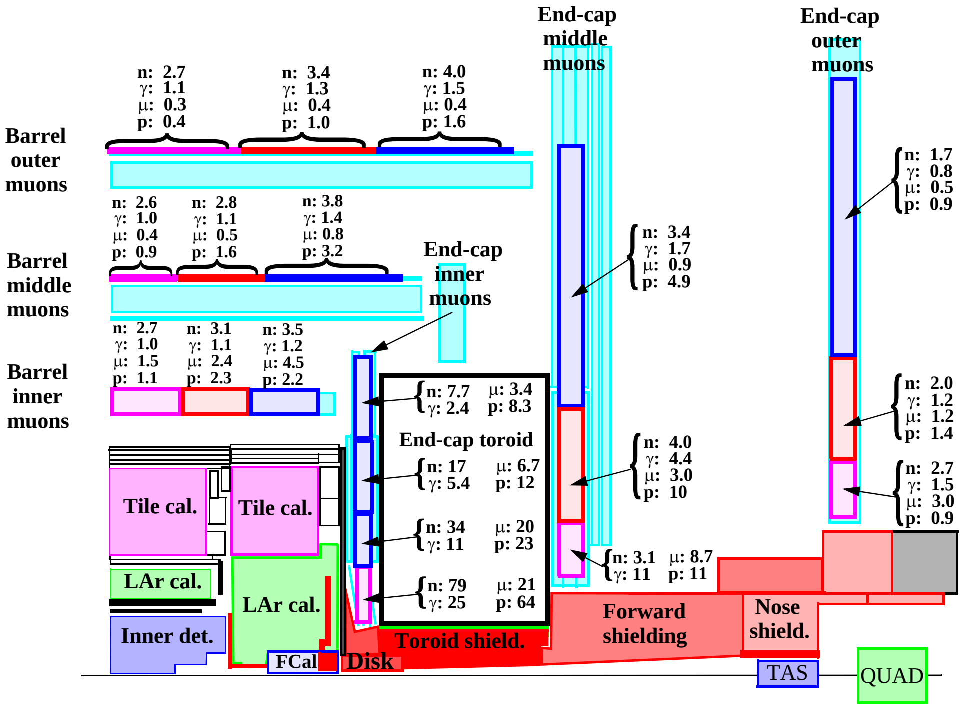

Figure 3.4: Particle fluxes in the various muon spectrometer stations at high luminosity (10^{34} cm^{-2} s^{-1}) as predicted by GCALOR. The neutron and photon fluxes are in units of kHz/cm^2 and the muon and proton fluxes in Hz/cm^2.

Signals in the detectors from background particles are the main issue, because these background signals may significantly reduce the muon track-finding efficiency and, more importantly, introduce large rates of fake triggers. The expected particle fluxes based on a simulation of the background radiation in the ATLAS muon spectrometer using the GCALOR program are shown in figure 3.4. The energy thresholds used in these simulations are 10 keV, 10^{-11} MeV (well below the thermal neutron energy range), 1 MeV, and 1 MeV for photons, neutrons, muons, and protons, respectively. The highest fluxes are expected in the innermost end-cap muon stations, in particular in the CSC's, which will have to cope with a large background counting rate, although the estimation of this rate is subject to systematic uncertainties between approximately 15% and 25%.

Background hit rates caused by neutrons and photons in the relevant energy range have been calculated with GEANT3 for all muon-chamber technologies using detailed geometrical descriptions of the muon chamber setup. Energy-dependent efficiency curves have been estimated for neutrons, photons, and electrons [34]. Calculations have been done for the various chamber types taking into account the angular distributions of the particles at the chamber locations. Fluxes tend to be isotropic in the barrel, while in the end-cap a substantial fraction of the particles originates from the interaction region and from the beam-pipe in the region of the end-cap toroids, which is the main local source of secondary radiation. The fake L1 trigger rate in the presence of these background hits was studied in simulation including large contingency factors to account for the various uncertainties in the predictions.

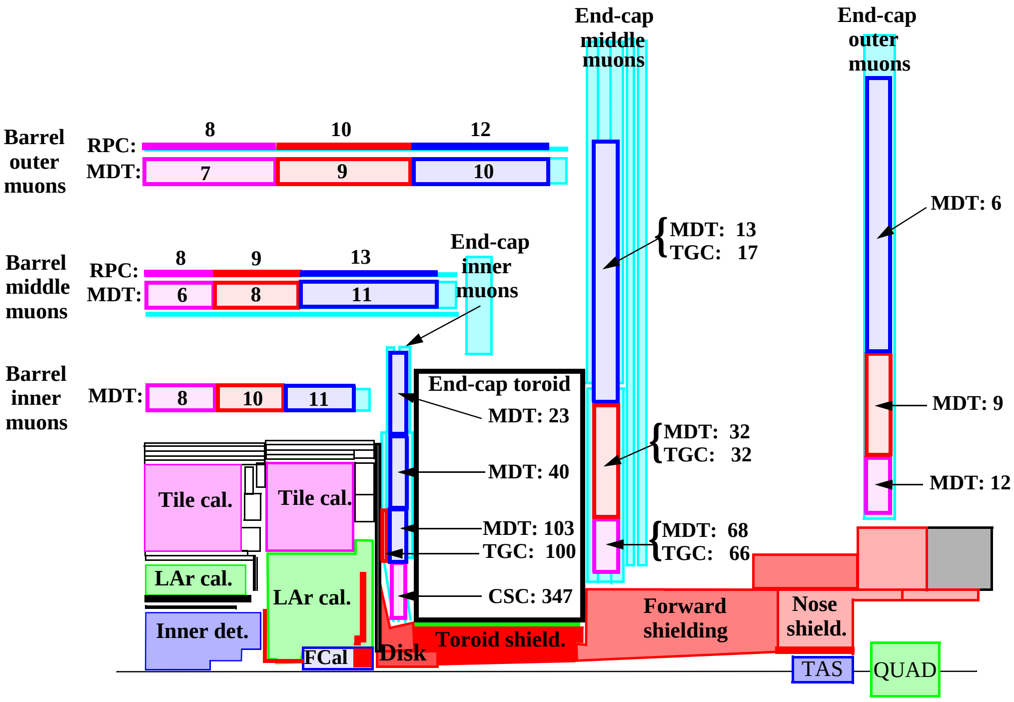

Figure 3.5: Average expected single-plane counting rates in Hz/cm^2 at 10^{34} cm^{-2} s^{-1} and for various regions in the muon spectrometer.

The single-plane efficiency curves have been compared between existing experimental data and simulation and found to be in good agreement. Average single-plane chamber efficiencies have been obtained by folding efficiency curves with the energy spectra predicted at each chamber location. Uncertainties due to the shape of the energy spectrum, the angular distribution, and the surrounding material have been studied and amount to a factor of 1.5. Predicted counting rates in the barrel stations are of the order of 10–12 Hz/cm^2 for both the MDT's and the resistive plate chambers. These rates are dominated by the photon contribution (80%), followed by neutrons and protons (10% each). In the inner barrel stations, the contribution from muons rises to about 15% and that from punch-through pions to a few percent. In the end-cap regions, photons contribute less to the counting rate. In the CSC's for example, photons account for about half of the rate, while muons account for 30% and protons for 10%. The predicted single-plane counting rates in the muon spectrometer are summarised in figure 3.5.

3.4 Background monitors

Measurements of particle fluences in ATLAS will provide a precise bench-marking of the particle transport codes used in the calculations and will also directly monitor the absorbed doses in the various detectors. Possible beam losses near the detector have to be monitored with specific detectors designed to provide fast feedback to the accelerator operations team. The motivation for equipping ATLAS with a reliable set of background monitors in various regions of the detector is therefore obvious.

2008 JINST 3 S08003

3.4.1 Monitors in the inner detector

The inner detector region of ATLAS contains a set of small detectors, which are sensitive to dose, to the 1 MeV neutron equivalent fluence (F_{neq}) and to thermal neutrons. These detectors consist of:

1. Field-effect transistors (RADFET's), which measure the total ionising dose;
2. PIN-diodes, which measure F_{neq};
3. Radiation-hardened transistors, which measure thermal neutron fluences.

These detectors will measure the integrated doses and fluences in the inner detector and will also to some extent provide bench-marking estimates of the different contributions (charged particles, neutrons and photons).

One of the worst-case scenarios during LHC operation arises if several proton bunches hit the collimators in front of the detectors. While the accumulated radiation dose from such unlikely accidents corresponds to that acquired during a few days of normal operation, and as such provides no major contribution to the integrated dose, the enormous instantaneous rate might cause detector damage. The ATLAS Beam Conditions Monitor (BCM) [54] system consists of a set of detectors designed to detect such incidents and trigger an abort in time to prevent serious damage to the detector (see also section 9.10). These incidents need to be distinguished from the stray protons and beam-gas backgrounds which frequently initiate charged particle showers, which originate well upstream (or downstream) from the ATLAS interaction point. Due to their very fast response time and intrinsically very high resistance to radiation, the BCM detectors will be used throughout the lifetime of the experiment to distinguish these stray beam particles from those originating from proton-proton interactions.

The BCM system, designed to tolerate doses of up to 500 kGy and in excess of 10^{15} charged particles per cm^2 over the lifetime of the experiment, consists of two stations, each with four modules. Each module, as depicted in figure 3.6 (left), includes two radiation-hard diamond sensors [55, 56] read out in parallel by radiation-tolerant electronics with a 1 ns rise-time [57]. Figure 3.6 (right) shows a close-up view of one station installed around the beryllium beam-pipe. The stations are located symmetrically around the interaction point at $z = \pm 184$ cm and $R = 5.5$ cm, which corresponds to a $|\eta| = 4.2$. The difference in time-of-flight between the two stations, Δt, distinguishes particles from normal collisions ($\Delta t = 0, 25, 50$ ns, etc.) from those arising from stray protons ($\Delta t = 12.5, 37.5$ ns, etc.). The in-time and out-of-time multi-module coincidences are determined by an FPGA-based back-end, which digitises the signals, monitors the detector performance and generates beam-abort signals if warranted. Preliminary analysis of data on one of the modules in a high-energy pion test-beam shows a signal-to-noise ratio of 11 ± 2 in an operational geometry, where minimum ionising particles are incident on the BCM sensors at a 45° angle. A full description of the design, construction and test-beam characterisation of the BCM system can be found in [54].

3.4.2 Monitors in the muon spectrometer

Several sets of detectors have been installed in the end-cap muon stations to monitor the background fluences and thus to constrain further the particle transport codes used in the calculations described

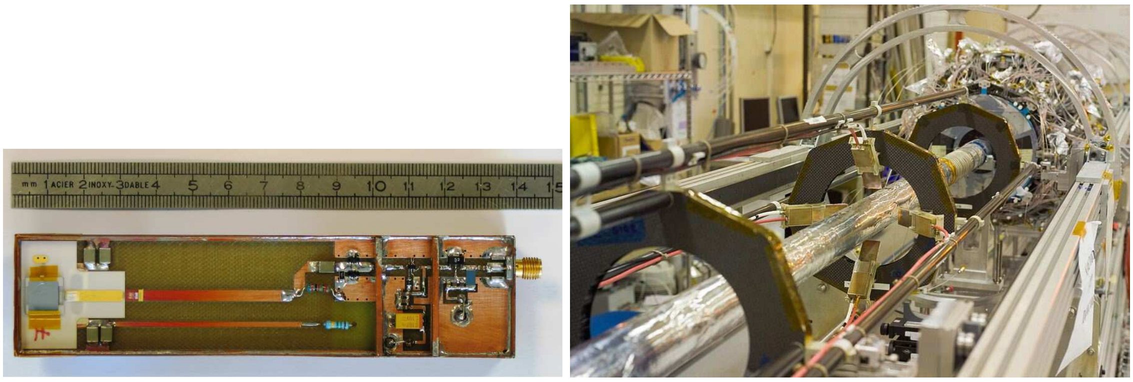

Figure 3.6: Left: top view of a BCM module, showing the diamond sensors (left side of picture), the HV supply and signal-transmission lines, the two amplification stages and the signal connector (right side of picture). Right: close-up view of one BCM station installed at 184 cm from the centre of the pixel detector, which can be seen at the far end of the picture. Each one of the four modules can be seen in position at a radius of 5.5 cm, very close to the beam-pipe.

in section 3.3. These detectors are installed in the inner, middle, and outer end-cap stations. Figure 3.7 shows one set of the detectors which have been installed. They were chosen to provide a reliable response to neutrons or photons in various energy ranges:

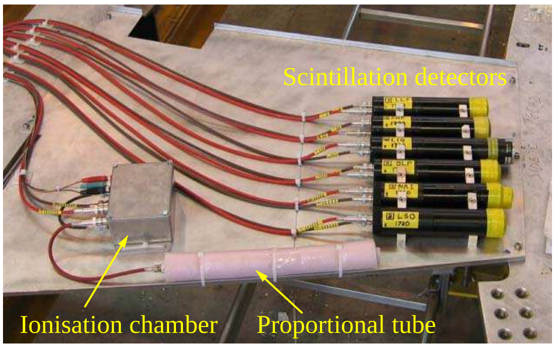

Figure 3.7: Picture of one set of background monitors, to be installed in the thin gap chamber layer of the middle end-cap muon station. The eight different types of detectors are described in the text.

1. Boron-lined proportional tubes operating with Ar/CO_2 gas are used to measure thermal and slow neutrons (energies below 10^{-5} MeV). Each interaction n + ^{10}B $\rightarrow$ Li + α sends a slow Li or α-particle into the tube. The large ionisation pulse associated with the Li or α-particle is used for pulse-height discrimination against Compton electrons and minimum-ionising particles. These detectors are therefore relatively insensitive to photons and charged particles.

2. Boron-loaded plastic scintillator (BC-454) is sensitive to the neutron interactions described above and is also used to study thermal and slow neutrons.

3. Detectors with a plastic disk loaded with LiF and coated with a thin layer of ZnS(Ag) scintillator are sensitive to the tritium and α-particles produced in the neutron capture process in lithium.

4. Another ZnS(Ag) scintillator embedded in plastic is used to study fast neutrons (with energies of a few MeV). The plastic is rich in hydrogen, from which incoming neutrons scatter to produce recoil protons. These protons produce large ionisation pulses compared to minimum-ionising particles or low-energy electrons. Pulse-height discrimination schemes should therefore provide good rejection against these backgrounds.

5. A liquid scintillator, with pulse-shape discrimination electronics, is used in combination with plastics to measure fast neutrons.

6. Scintillator detectors with NaI and lutetium oxyorthosilicate (LSO) crystals are used to measure the low-energy photon spectrum (0 to 10 MeV). The spectrum is dominated by photons, but also contains a neutron component, which can be separated out using fitting techniques and detailed simulations.

7. Small ionisation chambers measure the total ionising dose.

3.4.3 Network of detectors for radiation measurements

A system of small silicon pixel detectors has been developed for radiation measurements in the experimental environment [58, 59]. This detector network will form a stand-alone system fully capable of delivering real-time images of fluxes and spectral composition of different particle species, including slow and fast neutrons.

These silicon detectors will be operated via active USB cables and USB-ethernet extenders by a PC placed in the underground USA15 counting room, located next to the main cavern. The hybrid silicon pixel device consists of a silicon detector chip, 300 μm thick with 256×256 pixels, bonded to a readout chip. Each of the 55 μm$\times$55 μm pixels is connected to its respective readout chain integrated on the chip. Settings of the pulse height discriminators determine the input energy window and at the same time provide noise suppression. The pixel counter determines the number of interacting quanta of radiation falling within this window. These devices can be used for position and energy sensitive (from 5 keV up to tens of MeV) spectroscopic detection of radiation. They are also capable of counting particle fluxes at rates in excess of GHz/cm^2.

This system can be used in both tracking and counting modes, to record tracks or counts caused by x-rays, gamma-radiation, neutrons, electrons, minimum ionising particles and ions. For neutron detection, the silicon detectors are partially covered by neutron converters (^{6}LiF and polyethylene for slow and fast neutrons, respectively). The tracking mode is based on electronic visualisation of tracks and traces of individual quanta of radiation in the sensitive silicon volume. In the case of count rates above 5×10^3 events/cm^2 s, the devices are operated in counting mode, in which charge deposition in the pixels is counted at different threshold settings. Calibration of the devices enables the conversion of the individual tracks observed and/or counts measured into fluxes of respective types of radiation and dose rates. At least 14 of these pixel devices will be placed inside ATLAS: four devices on the LAr calorimeter facing the inner detector, four devices on the tile calorimeter, four devices near the muon chambers in the inner end-cap muon station, and two devices near the forward shielding and close to the outer end-cap muon station.

3.5 Activation

Induced radioactivity will be a major problem at the LHC, and ATLAS is the experiment with the highest levels of induced radiation. This is due to the small radius of the ATLAS beam-pipe, the small bore of the forward calorimeters, and to the shielding elements close to the beam-pipe. A comprehensive study has been made of the expected activation in different regions and for different data-taking and cooling-off scenarios. The methods and assumptions used in the calculation of the induced activity are given in [34]. The main conclusion of these studies is that the beam-pipe will be the major source of induced radioactivity in ATLAS.

Three different access scenarios are foreseen for ATLAS during shutdowns, as described in more detail in section 9.7. They are described below and two of the scenarios are depicted in figures 3.8 and 3.9.

(a) In the very short access scenario, all detector components remain in place and the magnetic fields remain on. These accesses are typically on the order of a few hours long.

(b) In the short access scenario, the beam-pipe remains in place, but then acts as a linear source of photon radiation as can be seen in figure 3.8. Because of the high level of radiation, the area around the beam-pipe, out to a radius of about 1 m, has to be fenced off after high-luminosity running. This will ensure that people working in ATLAS during short access will not be exposed to dose rates larger than 0.1 mSv/h (maintenance work in ATLAS will be designed to limit the yearly dose to 6 mSv per person). The only detector which is truly inside the barrier is the inner detector. During a short access, maintenance of the inner detector will therefore be severely limited.

(c) In the long access scenario, all the beam-pipe sections except the one inside the inner detector volume are removed as well as the small muon wheel (or inner end-cap muon stations) and the end-cap toroids. Two hot spots can clearly be seen in the final configuration, as shown in figure 3.9. One is the end-piece of the inner detector beam-pipe, which is made of aluminium, whereas the rest of the inner detector beam-pipe is made of beryllium. The expected dose rate can reach 0.2 mSv/h at this location. The other hot spot is in front of the forward calorimeters, where the dose rate is predicted to reach very high values of up to 0.5 mSv/h. These relatively small-size regions will therefore be temporarily shielded with lead blocks during maintenance of the inner detector.

While the beam-pipe section inside the inner detector is mostly made of beryllium, the rest of the beam-pipe is made of stainless steel and has to be removed in the case of the long access scenario, since it will become very radioactive with a contact dose rate of 3–5 mSv/h. This could in certain cases inflict several mSv of integrated dose to personnel performing the intervention. One way of reducing the dose to personnel would be to make the beam-pipe out of aluminium instead of stainless steel. This is expected to give a factor 10–50 reduction of the dose levels. If the beam-pipe material were instead to be changed to beryllium over the whole length of the detector, the dose rate would decrease by a factor of 100–1000 and would no longer be a problem. This is, however, very costly and will only be discussed further in the context of the LHC upgrade programme.

2008 JINST 3 S08003

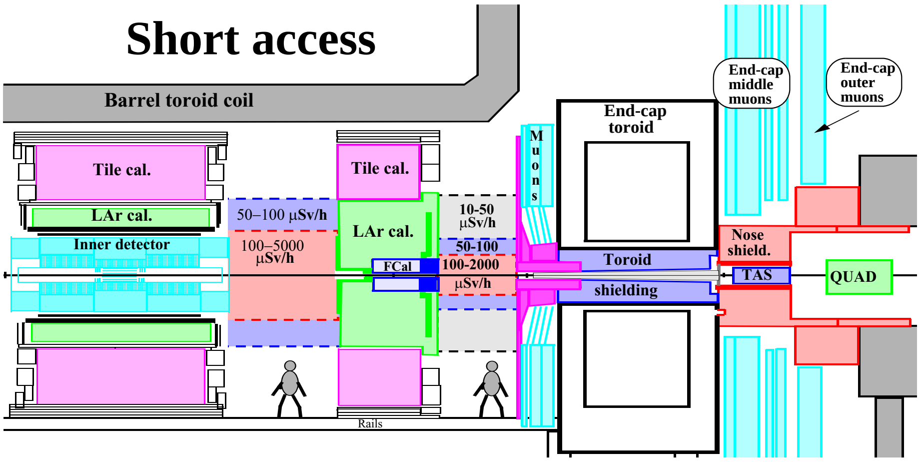

Figure 3.8: The inner region of the detector during one of the short access scenarios. The predicted dose rates have been calculated for 10 years of operation at 10^{34} cm^{-2} s^{-1} and for five days of cooling off. The short access scenario (a) has the beam-pipe in place.

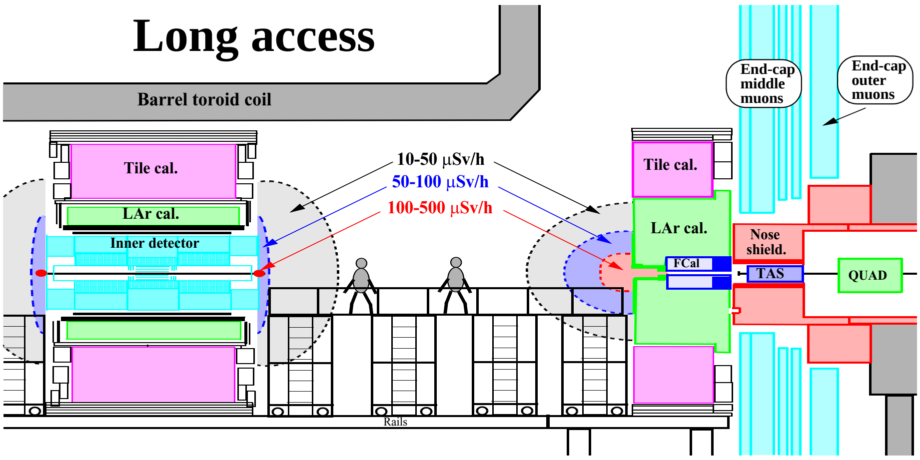

Figure 3.9: The inner region of the detector during one of the main long access scenarios. The predicted dose rates have been calculated for 10 years of operation at 10^{34} cm^{-2} s^{-1} and for five days of cooling off. The long access scenario (b) has only the inner detector section of the beam-pipe in place. The expected dose rates are greatly reduced in this access scenario.